Superchiral Light Generation on Degenerate Achiral Surfaces

Abraham Vázquez-Guardado[1,2] and Debashis Chanda[1,2,3,*]
[1]CREOL, College of Optics and Photonics, University of Central Florida, Orlando, Florida 32816, USA
[2]NanoScience Technology Center, University of Central Florida, Orlando, Florida 32826, USA
[3]Department of Physics, University of Central Florida, Orlando, Florida 32816, USA

(Received 20 October 2017; published 28 March 2018)

A novel route of superchiral near-field generation is demonstrated based on geometrically achiral systems supporting degenerate and spatially superimposed plasmonic modes. Such systems generate a single-handed chiral near field with simultaneous zero far-field circular dichroism. The phenomenon is theoretically elucidated with a rotating dipole model, which predicts a uniform single-handed chiral near field that flips handedness solely by reversing the handedness of the source. This property allows detection of pure background free molecular chirality through near-field light-matter interaction, which is experimentally demonstrated in the precise identification of both handedness of a chiral molecule on a single substrate with about four orders of magnitude enhancement in detection sensitivity compared to its conventional volumetric counterpart.

DOI: 10.1103/PhysRevLett.120.137601

Chirality is a ubiquitous property of life found in all biological systems, from fundamental left-handed amino acids and right-handed glucose, to the inherent chirality of complex DNA strands and proteins. Present in two enantiometric configurations: left (*sinister*, *s*-) and right (*dexter*, *d*-) [1], chiral molecules have undistinguishable physical properties and degenerate transition frequencies that do not allow their straightforward identification with common spectroscopic techniques. However, it is the interaction with other enantiomers that is the key to differentiate their intrinsic chiral configuration. Circularly polarized light (CPL), right polarized (RCP), or left polarized (LCP), is a classical example of an electromagnetic enantiomer pair that allows chiral light-matter interaction in circular dichroism (CD) spectroscopies. However, free propagating CPL has an upper chiral density bound that limits chiral light-matter interactions [2–4].

Recent efforts have been made to produce light fields with chiral density larger than CPL, called *superchiral* fields, using specially engineered fields. One approach is based on macroscopic interference produced by two counterpropagating CPL beams with opposite handedness to enhance the absorption rate of chiral molecules but at the cost of reducing electric field intensity [3,4]. Other alternative methods employ photonic [5–8] and plasmonic [9–25] surfaces to produce superchiral near fields [16–19,26–32]. Nevertheless, these systems produce a strong far-field CD signal that potentially overshadows weak molecular CD signals and low chiral near-field purity, i.e., similar contribution from both near-field handedness in the same volume. These mutually exclusive requirements were not accomplished in previous attempts based on macroscopic interference [3,4], geometrically chiral [17–20,30,31], or achiral [15,16,26–29] plasmonic substrates.

In this Letter, we demonstrate single-handed superchiral near-field generation on an achiral cavity-coupled plasmonic system, see Fig. 1(a), with simultaneous zero CD signal in the far field. The system supports two degenerate and superimposed orthogonal plasmonic modes that are simultaneously excited with CPL with the corresponding phase difference between each other resulting in an effective rotating resonance. The coherent interaction between the localized surface plasmon and the cavity

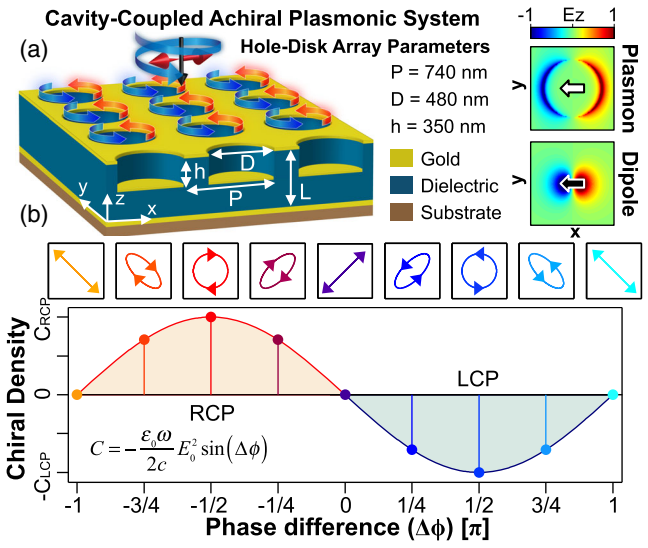

FIG. 1. (a) (Left) Achiral plasmonic system, comprised of a cavity-coupled hole-disk array, which supports rotating dipolar resonance when excited with CPL. (Right) Out-of-plane electric field comparing the LSPR and dipole modes. (b) Chiral density of a plane wave with arbitrary polarization state propagating along the -*z* direction (into the paper).

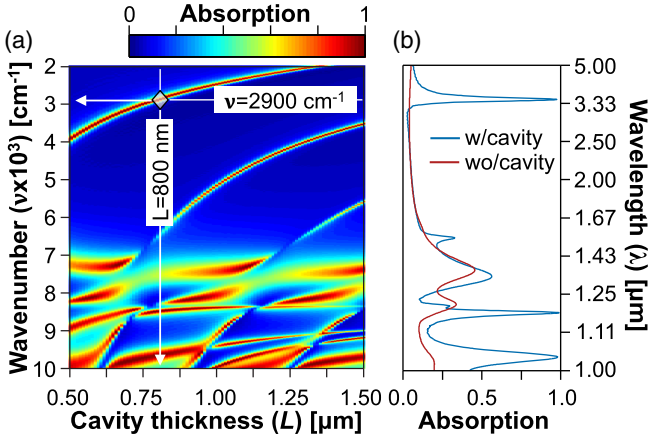

FIG. 2. (a) Cavity absorption dispersion for normal excitation with LP light. (b) Absorption spectra comparison for a cavity thickness of $L = 800$ nm and a cavity-uncoupled hole disk.

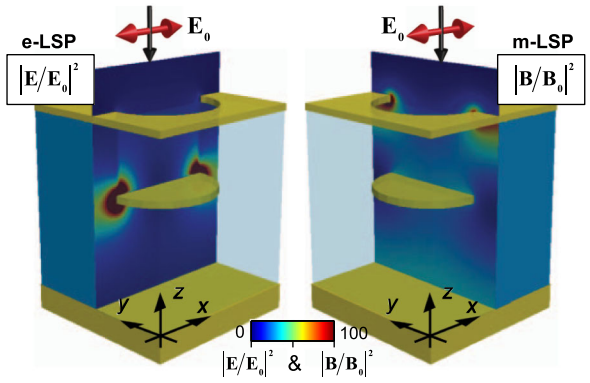

FIG. 3. Electric (left) and magnetic (right) intensity cross section at the center of one unit cell for $L = 800$ nm and $\nu = 2900$ cm^{-1}.

enhances the otherwise weak uncoupled-plasmonic resonance and produces the superchiral near field [33–35]. The physical phenomenon that allows this exceptional effect is elucidated with an achiral oscillating point dipole model, which accurately agrees with the finite difference time domain (FDTD) predicted plasmonic modal behavior. It is found that the spatiotemporal distribution of the rotating resonance, and not the field distribution *per se*, is the true mechanism of this unique superchiral near field generation. Finally, we experimentally demonstrate, for the first time, vibrational circular dichroism (VCD), where both chiral enantiomers are accurately identified at very low concentration ~3.8 nL volume with 3 wt% molecular filling fraction on a single achiral plasmonic substrate.

The spatial distribution of the electromagnetic chiral density of an arbitrary complex field, whether in the near field or far field, related to the spin angular momentum and helicity of light [36–38], is given by [2,4]

$$C(\mathbf{r}) = -\frac{1}{2}\varepsilon_0\omega \mathrm{Im}(\mathbf{E}^* \cdot \mathbf{B}) \tag{1}$$

where $\mathbf{E}$ and $\mathbf{B}$ are the complex time varying electric and magnetic field vectors, $\mathbf{r}$ is the position vector, and ε_0 is the vacuum permittivity. As stated by Eq. (1), it is the collinear configuration with nonzero phase difference between the electric and magnetic fields that produces a finite value of chiral density. For a backward propagating plane wave, $\mathbf{E} = (1/\sqrt{2})E_0(\hat{x} + e^{i\Delta\phi}\hat{y})e^{-i(\omega t - \mathbf{k}\cdot\mathbf{r})}$, $\mathbf{B} = (\mathbf{k} \times \mathbf{E})/\omega$ and $\mathbf{k} = -k\hat{z}$, where k is the free space wave vector, E_0 the electric field magnitude, and $\Delta\phi$ the phase between the orthogonal field vectors, the chiral density becomes $C(\mathbf{r}) = -(\varepsilon_0\omega/2c)E_0^2 \sin(\Delta\phi)$, where c is the speed of light in vacuum. It is clearly evident that a linearly polarized (LP) plane wave ($\Delta\phi = 0$) does not carry chiral density since the transverse $\mathbf{E}$ and $\mathbf{B}$ fields are always orthogonal; see Fig. 1(b). This is not the scenario for CPL whose chiral density is $C_{\mathrm{CPL}} = -\pm(\varepsilon_0\omega/2c)E_0^2$: $C_{\mathrm{LCP}} < 0$ ($\Delta\phi = +\pi/2$) and $C_{\mathrm{RCP}} > 0$ ($\Delta\phi = -\pi/2$). Any arbitrary polarization state will render lower chiral densities than CPL, yet retaining the corresponding helicity determined by the phase difference as observed in Fig. 1(b).

The proposed achiral plasmonic substrate is illustrated in Fig. 1(a), which is comprised of a nanostructured square array of gold hole disks ($P = 740$ nm, $D = 480$ nm, hole-disk separation $h = 350$ nm, and film thickness of 30 nm) coupled with an asymmetric Fabry-Perot cavity. The cavity is formed with a gold back reflector separating the plasmonic pattern with cavity thickness (L) determined by the dielectric film. In order to understand the electromagnetic properties of this coupled system we performed finite difference time domain (FDTD) simulations; see Supplemental Material [39]. Figure 2(a) shows the absorption dispersion for LP excitation. The first interaction, yet not the scope of this work, occurs around 9700 – 7000 cm^{-1} where the hole-disk system supports natural localized surface plasmon (LSP) modes induced solely by the geometrical parameters of the array. In this band hybrid resonance modes are observed as absorption frequency splitting around the LSP absorption band due to the coherent interaction between cavity and plasmonic modes [33,34].

A second, yet more interesting, interaction occurs when the cavity resonates away from the natural LSP band of the top plasmonic pattern. The cavity resonance depends strictly on the propagation phase imposed by the cavity ($n_d kL$), where n_d is the refractive index of the dielectric spacer. Although adding a cavity enhances the LSP mode at the natural LSP band compared to its uncoupled counterpart [33], the excitation of LSP modes at lower energies is possible when placing a polarizable element inside the cavity [43] as observed in the absorption spectra in Fig. 2(b). At the fundamental cavity resonant mode the electric field antinodes are located around the optical center of the cavity where the disk is placed, while strong magnetic field antinodes are located at the edges of the

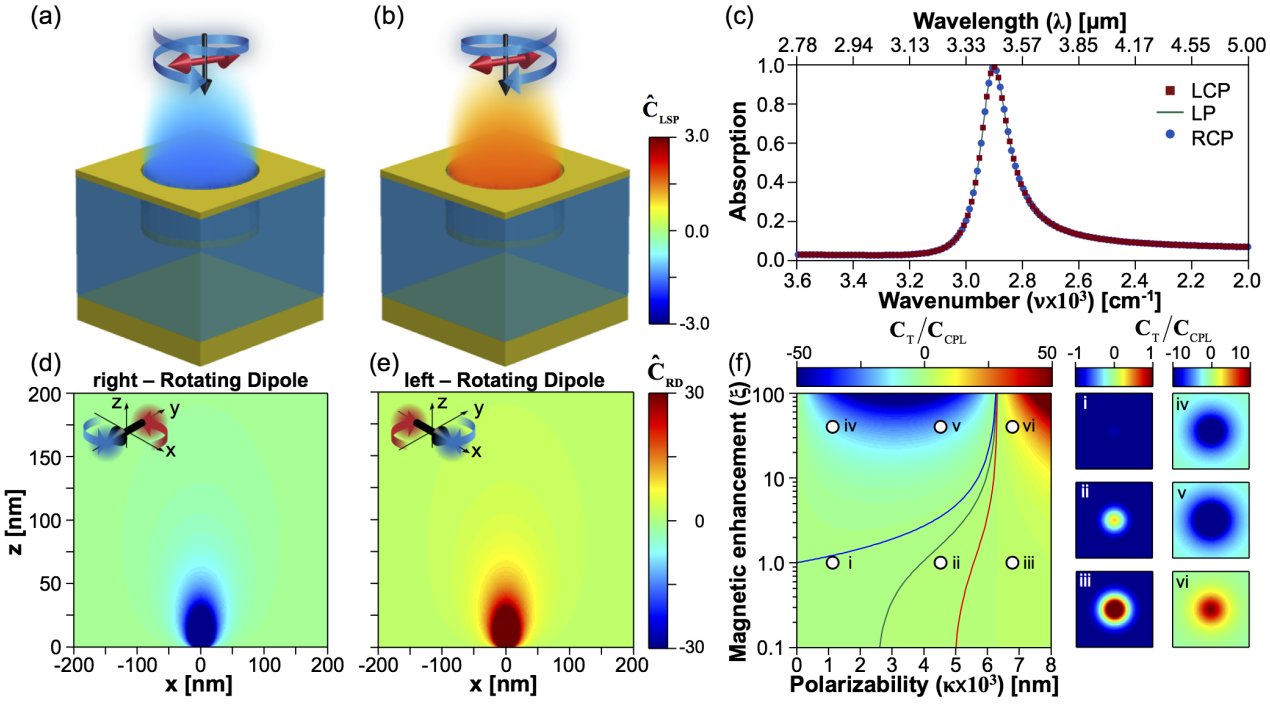

FIG. 4. Free space normalized LSP chiral near-field density distribution for LCP (a) and RCP (b) excitations, represented in one array unit cell. (c) Simulated absorption spectra of the 2D achiral plasmonic substrate for LCP, LP, and RCP. Chiral near field cross section for (d) right RD and (e) left RD with $\kappa = 2.8 \times 10^3$ nm^2 and $\xi = 20$. (f) Near field chiral density at $(x, y) = 0$ and $z_0 = 50$ nm produced by the backward propagating LCP ($C < 0$) incident field and the excited dipole field. Right panel represents the chiral field in the xy plane at $z_0 = 50$ nm for $(\kappa \times 10^3, \xi)$: i (1.1, 1), ii (4.5, 1), iii (6.7, 1), iv (1.1, 40), v (4.5, 40), vi (6.7, 40).

cavity, i.e., the back reflector and the top hole array. As a result, the cavity selectively polarizes the hole-disk system inducing electric or magnetic LSP modes (e-LSP or m-LSP) on the disk or hole, respectively, as observed in Fig. 3.

This symmetric achiral system supports two degenerate LSP resonances along each of the lattice axes. Upon illumination with CPL both LSP modes are excited simultaneously with a phase difference imposed by the excitation source. Both electric and magnetic field intensity distributions are exactly the same when excited either by LCP or RCP, see Fig. S1(a) [39], without any dissymmetry in the absorption spectrum; see Fig. 4(c). However, the chiral near-field density generated by this system is remarkably different. As observed in Figs. 4(a) and 4(b), the near-field chiral density has the same handedness as the incident light which fully reverses when flipping the incident CPL excitation on the same geometry. Furthermore, volume integration in the upper half-space of the unit cell at resonance reveals 99.96% of the near field has CPL-like chiral density and only 0.04% has the opposite helicity across the entire LSP band; see Fig. S2 [39]. This is not the case for LP where the chiral near-field volume average is zero as both helicities are present; see Figs. S1(a) and S2 [39].

The aforementioned property is phenomenologically modeled using a rotating dipole (RD); see Fig. S3 [39]. The plasmonic system, when excited with CPL, produces a spatiotemporal rotating motion along the optical axis making the rotating dipole model suitable for the present context. The RD oriented in the xy plane at $z = 0$ is $\tilde{\mathbf{p}} = p_0 \hat{\mathbf{p}} e^{-i\omega t} = (1/\sqrt{2}) p_0 (\hat{x} + e^{i\Delta\phi}\hat{y}) e^{-i\omega t}$, where p_0 is the dipole moment magnitude and ω is the angular frequency. A right (left) RD corresponds to a phase difference of $+(-)\pi/2$ [39]. The corresponding electric and magnetic fields associated with this dipole are $\mathbf{E}_{\mathrm{RD}}(\mathbf{r}) = (1/4\pi\varepsilon_0)(e^{ikr}/r^3)\{k^2 r^2 (\mathbf{n} \times \tilde{\mathbf{p}}) \times \mathbf{n} + [3\mathbf{n}(\mathbf{n} \cdot \tilde{\mathbf{p}}) - \tilde{\mathbf{p}}](1 - ikr)\}$, and $\mathbf{B}_{\mathrm{RD}}(\mathbf{r}) = \xi(c\mu_0 k^2/4\pi)(e^{ikr}/r)(\mathbf{n} \times \tilde{\mathbf{p}})[1 - (1/ikr)]$ [40]. Here $\mathbf{n}$ is the unit vector and $\mathbf{r}$ is the position vector with magnitude r. In addition, an enhancement factor ξ is introduced in the magnetic field. This empirical variable quantifies the common misbalance in the magnetic to electric near-field enhancement factors on plasmonic systems at resonance.

Solving Eq. (1) for this set of vector fields we obtain that the spatial dependence of the RD chiral near-field density is

$$C_{\mathrm{RD}}(\mathbf{r}) = C_{\mathrm{RD0}} \sin(\Delta\phi) \frac{z}{r^3}, \tag{2}$$

were C_{RD0} is a scale factor given by the dipole electromagnetic parameters [39]. From this simple result we can make three important observations: for a fixed rotation direction $\Delta\phi$ the chiral near field in the entire upper stratum, $z > 0$, has same chirality sign that fully reverses uniquely by

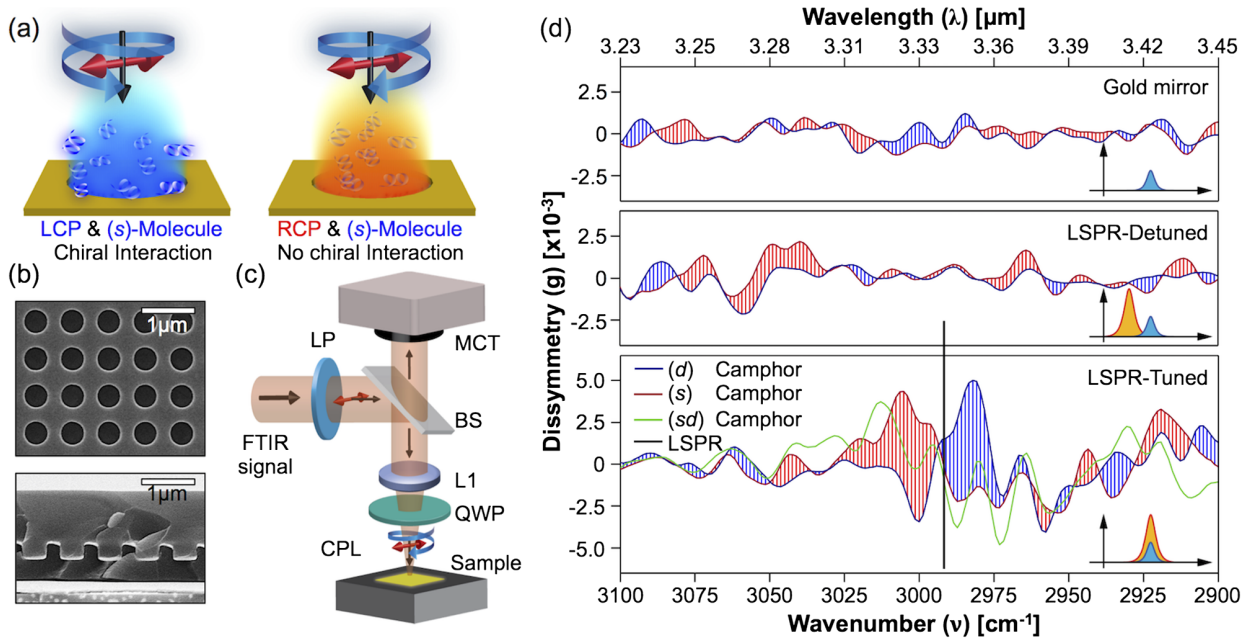

FIG. 5. (a) Schematic representation of chiral light-matter interaction between LCP and (*s*) enantiomer. (b) Top view of one uncoated sample and cross section view of one polymer coated substrate embedding the chiral molecule. (c) Experimental representation for the optical characterization. (d) Dissymmetry factor for camphor (from top to bottom) on planar gold mirror, detuned, and tuned achiral plasmonic substrate (also illustrated in the inset of each plot). Vertical line represents the LSPR of the tuned substrate.

flipping the rotation direction of the dipole $\Delta\phi$; the chirality of a linear dipole is zero; and the chiral field is strictly confined in the near-field around the dipole oscillation center as seen in Fig. S4 [39].

Finally, the total chiral near-field is obtained by including the total field, i.e., $\mathbf{E}_T = \mathbf{E}_{\mathrm{CPL}} + \mathbf{E}_{\mathrm{RD}}$ and $\mathbf{B}_T = \mathbf{B}_{\mathrm{CPL}} + \mathbf{B}_{\mathrm{RD}}$. The contribution to the total chiral density, $C_T = C_{\mathrm{CPL}} + C_{\mathbf{E}\mathrm{CPL}-\mathbf{B}\mathrm{RD}} + C_{\mathbf{E}\mathrm{RD}-\mathbf{B}\mathrm{CPL}} + C_{\mathrm{RD}}$, originates from four sources: the incident field (C_{CPL}) and RD (C_{RD}), as previously described, and the interaction from the incident electric or magnetic field with the dipole-generated magnetic or electric field ($C_{\mathbf{E}\mathrm{CPL}-\mathbf{B}\mathrm{RD}}/C_{\mathbf{E}\mathrm{RD}-\mathbf{B}\mathrm{CPL}}$). Solving the electromagnetic chirality for these two extra terms the total chirality becomes

$$C_T(\mathbf{r}) = C_{\mathrm{CPL}}\left\{1 + \frac{\kappa}{r^3}\left[\xi z + \frac{1}{2r}(r^2 - 3z^2) - \xi k^2 \kappa z\right]\right\}, \tag{3}$$

where $\kappa = \alpha_0 k/4\pi\varepsilon_0$ is the normalized dipole polarizability and α_0 is the dipole polarizability, see the Supplemental Material for full result as a function of $\Delta\phi$ [39]. It is clear that both polarizability and magnetic field enhancement have significant effect to the total chiral near-field. Consider Eq. (3) for $(x, y) = 0$, $r = z$ and $z > 0$ plotted in Fig. 4(f), left panel and xy planes for $z = z_0$ and representative (κ, ξ) plotted in Fig. 4(f), right panel. The condition for ξ that produces zero chiral density is $\xi_{\mathrm{th}} = (1 - \kappa^{-1} r^2)(1 - k^2\kappa)^{-1}$ determining the threshold at which the chiral density flips sign with respect to the incident field [green line in Fig. 4(f) and conditions *i* and *ii*]. It also determines the nature of the total chiral density. If $\xi > \xi_{\mathrm{th}}$, the dipole magnetic field dominates ($C_{\mathbf{E}\mathrm{CPL}-\mathbf{B}\mathrm{RD}}$) observed in condition *i* compared to *ii* for $\xi < \xi_{\mathrm{th}}$. In addition, if $\xi > (1 - k^2\kappa)^{-1}$, the total near field becomes superchiral [blue line in Fig. 4(f) and conditions *iv* and *v*]. On the other hand, if $\xi < \xi_{\mathrm{th}}$ the dipole electric field dominates ($C_{\mathbf{E}\mathrm{RD}-\mathbf{B}\mathrm{CPL}}$) reversing the chiral density sign with respect to the incident field with superchiral light generation condition when $\xi < (1 - 2\kappa^{-1} r^2)(1 - k^2\kappa)^{-1}$ [red line in Fig. 4(f) and conditions *iii* and *vi*].

This RD model reveals the true nature of the chiral near field generated by the dipolelike LSP mode excited in our achiral plasmonic system. As observed in Fig. 3, the *m*-LSP dominates the resonance on the top hole over the *e*-LSP mode establishing the condition of weak electric polarizability but large magnetic field enhancement. The spatial chiral density profile (xz for $y = 0$) for such a RD is plotted in Figs. 4(e) for right RD and left RD, respectively. In this result a centrosymmetric chiral density profile is observed on top of the RD dipole [Fig. 4(f)]. As observed in Fig. S1(a) [39] it is not the LSP field distribution *per se* that produces single-handed chiral near fields but its spatiotemporal distribution of the rotating degenerate resonance, which was not the case in a symmetric, yet achiral, configuration [27]. Finally, the effective rotating LSP mode produces twisted Poynting vectors swirling into the hole. As a result, an optical vortex is generated demonstrating the existence of

orbital angular momentum. Hence, the local field helicity along with the twisted phase fronts must conserve the total incident angular momentum [36].

The absorption dissymmetry for an arbitrary molecule is determined by both matter and light chirality [44]. While matter chirality is fixed for a particular molecule, it is only the electromagnetic chirality that enhances the scattered far-field CD signal, defined as $g = 2(R^{\mathrm{RCP}} - R^{\mathrm{LCP}})/(R^{\mathrm{RCP}} + R^{\mathrm{LCP}})$. The proposed system is achiral and hence does not change the overall geometrical chirality (molecule + device). However, it advantages from the fact that it is able to exploit both chirality as well as the enhanced superchiral near field at the hot spots localized around the patterned area, which concomitantly enhances the light-matter interaction. We demonstrate surface enhanced vibrational chiral dichroism, pictographically represented in Fig. 5(a), in our proposed achiral plasmonic substrate tuned the C-H vibrational band of camphor, $\nu \sim 3000\ \mathrm{cm}^{-1}$. The chiral molecules are embedded in a polymer matrix solution at ~0.614 M concentration, spun coated onto the substrate to form a thin film with an approximate 3% molecular filling fraction as observed in Fig. 5(b). The optical characterization is performed using a microscope-coupled FTIR probing a volume of ~3.8 nL, see the Supplemental Material [39]. The optical configuration is schematically shown in Fig. 5(c).

The dissymmetry in the reflectance (g) for (d) camphor and (s) camphor is shown in Fig. 5(d), where $g \sim 5 \times 10^{-3}$ is observed around the LSP resonance, represented by the vertical line in Fig. 5(d). In contrast, the same films deposited and characterized on a flat gold film and on the same achiral plasmonic substrate detuned from the camphor absorption band do not show dissymmetry in the reflectance spectra; see Fig. 5(d). Therefore, it is the chiral near field generated by the plasmon resonance, which further overlaps with the absorption band of the chiral analyte, that give rise to a finite VCD signal since it is at resonance where the chiral near-field density is maximum. Conventional VCD spectroscopy of 0.6 M camphor in liquid solvent [45] reveals path length normalized dissymmetry factors (g/μm) in the order of $2 \times 10^{-7}\ \mu\mathrm{m}^{-1}$. In contrast, our demonstration on a similar concentration but much smaller effective path length of ~1 μm, dissymmetry factors of $g \sim 5 \times 10^{-3}\ \mu\mathrm{m}^{-1}$ is observed, with about 4 orders of magnitude enhancement in detection sensitivity (g/μm). According to our simulations, the achiral plasmonic structure offers superchiral near-field generation through the magnetic plasmon resonance. This is a limiting factor in the current demonstration since the chiral molecular absorption rate is predominantly defined by electric dipole transitions.

In this Letter, we present a novel way to generate a single-handed superchiral near field on achiral plasmonic substrates with simultaneous zero far-field CD. The fundamental physical mechanism is theoretically elucidated using a rotating dipole model and experimentally demonstrated in surface-enhanced VCD on a single achiral substrate. The proposed concept removes the constraint in surface-enhanced chiroptical spectroscopy requiring both chiral plasmonic enantiomers to perform enantiomeric discrimination. We envisage the result of this work will promote further fundamental and applied research in biosensing, where not only the detection of the target analyte would be possible, but its chiral configuration like real time monitoring of protein folding as well.

This research work was supported by the Florida Space Institute/NASA (63018092), Northrop Grumman Corporation (63018088) and DARPA (WIRED, HR0011-16-1-0003). A. V. G. acknowledges the Consejo Nacional de Ciencia y Tecnología (CONACyT) and the Secretaría de Educación Pública (SEP).

*debashis.chanda@creol.ucf.edu

[1] D. B. Amabilino, *Chirality at the Nanoscale* (Wiley-VCH, Weinheim, Germany, 2009), DOI: 10.1002/9783527625345.
[2] D. M. Lipkin, J. Math. Phys. (N.Y.) **5**, 696 (1964).
[3] Y. Tang and A. E. Cohen, Science **332**, 333 (2011).
[4] Y. Tang and A. E. Cohen, Phys. Rev. Lett. **104**, 163901 (2010).
[5] A. Papakostas, A. Potts, D. M. Bagnall, S. L. Prosvirnin, H. J. Coles, and N. I. Zheludev, Phys. Rev. Lett. **90**, 107404 (2003).
[6] A. S. Schwanecke, A. Krasavin, D. M. Bagnall, A. Potts, A. V. Zayats, and N. I. Zheludev, Phys. Rev. Lett. **91**, 247404 (2003).
[7] S. L. Prosvirnin and N. I. Zheludev, Phys. Rev. E **71**, 037603 (2005).
[8] M. Reichelt, S. W. Koch, A. V. Krasavin, J. V. Moloney, A. S. Schwanecke, T. Stroucken, E. M. Wright, and N. I. Zheludev, Appl. Phys. B **84**, 97 (2006).
[9] M. Decker, M. W. Klein, M. Wegener, and S. Linden, Opt. Lett. **32**, 856 (2007).
[10] M. Decker, M. Ruther, C. E. Kriegler, J. Zhou, C. M. Soukoulis, S. Linden, and M. Wegener, Opt. Lett. **34**, 2501 (2009).
[11] J. K. Gansel, M. Wegener, S. Burger, and S. Linden, Opt. Express **18**, 1059 (2010).
[12] S. V. Zhukovsky, C. Kremers, and D. N. Chigrin, Opt. Lett. **36**, 2278 (2011).
[13] D. N. Chigrin, C. Kremers, and S. V. Zhukovsky, Appl. Phys. B **105**, 81 (2011).
[14] F. Eftekhari and T. J. Davis, Phys. Rev. B **86**, 075428 (2012).
[15] M. H. Alizadeh and B. M. Reinhard, ACS Photonics **2**, 361 (2015).
[16] T. J. Davis and E. Hendry, Phys. Rev. B **87**, 085405 (2013).
[17] N. Meinzer, E. Hendry, and W. L. Barnes, Phys. Rev. B **88**, 041407 (2013).
[18] M. Schäferling, N. Engheta, H. Giessen, and T. Weiss, ACS Photonics **3**, 1076 (2016).

[19] E. Hendry, R. V. Mikhaylovskiy, L. D. Barron, M. Kadodwala, and T. J. Davis, Nano Lett. **12**, 3640 (2012).
[20] E. Hendry, T. Carpy, J. Johnston, M. Popland, R. V. Mikhaylovskiy, A. J. Lapthorn, S. M. Kelly, L. D. Barron, N. Gadegaard, and M. Kadodwala, Nat. Nanotechnol. **5**, 783 (2010).
[21] B. Frank, X. Yin, M. Schäferling, J. Zhao, S. M. Hein, P. V. Braun, and H. Giessen, ACS Nano **7**, 6321 (2013).
[22] R. Tullius, A. S. Karimullah, M. Rodier, B. Fitzpatrick, N. Gadegaard, L. D. Barron, V. M. Rotello, G. Cooke, A. Lapthorn, and M. Kadodwala, J. Am. Chem. Soc. **137**, 8380 (2015).
[23] M. Hentschel, V. E. Ferry, and A. P. Alivisatos, ACS Photonics **2**, 1253 (2015).
[24] V. K. Valev, J. J. Baumberg, C. Sibilia, and T. Verbiest, Adv. Mater. **25**, 2517 (2013).
[25] J. T. Collins, C. Kuppe, D. C. Hooper, C. Sibilia, M. Centini, and V. K. Valev, Adv. Opt. Mater. **5**, 1700182 (2017).
[26] X. Tian, Y. Fang, and M. Sun, Sci. Rep. **5**, 17534 (2015).
[27] M. Schäferling, X. Yin, and H. Giessen, Opt. Express **20**, 26326 (2012).
[28] A. García-Etxarri and J. A. Dionne, Phys. Rev. B **87**, 235409 (2013).
[29] S. Yoo, M. Cho, and Q.-H. Park, Phys. Rev. B **89**, 161405 (2014).
[30] M. Schäferling, D. Dregely, M. Hentschel, and H. Giessen, Phys. Rev. X **2**, 031010 (2012).
[31] M. Schäferling, X. Yin, N. Engheta, and H. Giessen, ACS Photonics **1**, 530 (2014).
[32] M. L. Nesterov, X. Yin, M. Schäferling, H. Giessen, and T. Weiss, ACS Photonics **3**, 578 (2016).
[33] A. Vázquez-Guardado, A. Safaei, S. Modak, D. Franklin, and D. Chanda, Phys. Rev. Lett. **113**, 263902 (2014).
[34] D. Chanda, K. Shigeta, T. Truong, E. Lui, A. Mihi, M. Schulmerich, P. V. Braun, R. Bhargava, and J. A. Rogers, Nat. Commun. **2**, 479 (2011).
[35] A. Safaei, S. Chandra, A. Vázquez-Guardado, J. Calderon, D. Franklin, L. Tetard, L. Zhai, M. N. Leuenberger, and D. Chanda, Phys. Rev. B **96**, 165431 (2017).
[36] M. M. Coles and D. L. Andrews, Phys. Rev. A **85**, 063810 (2012).
[37] K. Y. Bliokh and F. Nori, Phys. Rev. A **83**, 021803 (2011).
[38] S. M. Barnett, R. P. Cameron, and A. M. Yao, Phys. Rev. A **86**, 013845 (2012).
[39] See Supplemental Material at http://link.aps.org/supplemental/10.1103/PhysRevLett.120.137601 for more information on fabrication, characterization, and simulation methods; supporting FDTD calculations; and detailed theoretical calculations; which includes Refs. [27,40–42].
[40] J. D. Jackson, *Classical Electrodynamics*, 3rd ed. (John Wiley & Sons, New York, 2007).
[41] E. D. Palik *Handbook of Optical Constants of Solids* (Academic Press, New York, 1985).
[42] J. Ahrens, B. Geveci, and C. Law, *Visualization Handbook* (Elsevier, Massachusetts, 2005).
[43] E. T. Jaynes and F. W. Cummings, Proc. IEEE **51**, 89 (1963).
[44] L. D. Barron, *Molecular Light Scattering and Optical Activity*, 2nd ed. (Cambridge University Press, Cambridge, England, 2004).
[45] C. Guo, R. D. Shah, R. K. Dukor, T. B. Freedman, X. Cao, and L. A. Nafie, Vib. Spectrosc. **42**, 254 (2006).